

EUROPEAN ORGANIZATION FOR NUCLEAR RESEARCH

CERN-EP-2001-064

31 August 2001

Measurement of the Hadronic Cross-Section for the Scattering of Two Virtual Photons at LEP

The OPAL Collaboration

Abstract

The interaction of virtual photons is investigated using the reaction $e^+e^- \rightarrow e^+e^-$ hadrons based on data taken by the OPAL experiment at e^+e^- centre-of-mass energies $\sqrt{s_{ee}} = 189 - 209$ GeV, for $W > 5$ GeV and at an average Q^2 of 17.9 GeV 2 . The measured cross-sections are compared to predictions of the Quark Parton Model (QPM), to the Leading Order QCD Monte Carlo model PHOJET to the NLO prediction for the reaction $e^+e^- \rightarrow e^+e^- q\bar{q}$, and to BFKL calculations. PHOJET, NLO $e^+e^- \rightarrow e^+e^- q\bar{q}$, and QPM describe the data reasonably well, whereas the cross-section predicted by a Leading Order BFKL calculation is too large.

(Submitted to European Physical Journal C)

The OPAL Collaboration

G. Abbiendi², C. Ainsley⁵, P.F. Åkesson³, G. Alexander²², J. Allison¹⁶, G. Anagnostou¹, K.J. Anderson⁹, S. Arcelli¹⁷, S. Asai²³, D. Axen²⁷, G. Azuelos^{18,a}, I. Bailey²⁶, E. Barberio⁸, R.J. Barlow¹⁶, R.J. Batley⁵, T. Behnke²⁵, K.W. Bell²⁰, P.J. Bell¹, G. Bella²², A. Bellerive⁹, S. Bethke³², O. Biebel³², I.J. Bloodworth¹, O. Boeriu¹⁰, P. Bock¹¹, J. Böhme²⁵, D. Bonacorsi², M. Boutemeur³¹, S. Braibant⁸, L. Brigliadori², R.M. Brown²⁰, H.J. Burckhart⁸, J. Cammin³, R.K. Carnegie⁶, B. Caron²⁸, A.A. Carter¹³, J.R. Carter⁵, C.Y. Chang¹⁷, D.G. Charlton^{1,b}, P.E.L. Clarke¹⁵, E. Clay¹⁵, I. Cohen²², J. Couchman¹⁵, A. Csilling^{8,i}, M. Cuffiani², S. Dado²¹, G.M. Dallavalle², S. Dallison¹⁶, A. De Roeck⁸, E.A. De Wolf⁸, P. Dervan¹⁵, K. Desch²⁵, B. Dienes³⁰, M.S. Dixit^{6,a}, M. Donkers⁶, J. Dubbert³¹, E. Duchovni²⁴, G. Duckeck³¹, I.P. Duerdorff¹⁶, E. Etzion²², F. Fabbri², L. Feld¹⁰, P. Ferrari¹², F. Fiedler⁸, I. Fleck¹⁰, M. Ford⁵, A. Frey⁸, A. Fürtjes⁸, D.I. Futyan¹⁶, P. Gagnon¹², J.W. Gary⁴, G. Gaycken²⁵, C. Geich-Gimbel³, G. Giacomelli², P. Giacomelli², D. Glenzinski⁹, J. Goldberg²¹, K. Graham²⁶, E. Gross²⁴, J. Grunhaus²², M. Gruwé⁸, P.O. Günther³, A. Gupta⁹, C. Hajdu²⁹, M. Hamann²⁵, G.G. Hanson¹², K. Harder²⁵, A. Harel²¹, M. Harin-Dirac⁴, M. Hauschild⁸, J. Hauschildt²⁵, C.M. Hawkes¹, R. Hawkings⁸, R.J. Hemingway⁶, C. Hensel²⁵, G. Herten¹⁰, R.D. Heuer²⁵, J.C. Hill⁵, K. Hoffman⁹, R.J. Homer¹, D. Horváth^{29,c}, K.R. Hossain²⁸, R. Howard²⁷, P. Hüntemeyer²⁵, P. Igo-Kemenes¹¹, K. Ishii²³, A. Jawahery¹⁷, H. Jeremie¹⁸, C.R. Jones⁵, P. Jovanovic¹, T.R. Junk⁶, N. Kanaya²⁶, J. Kanzaki²³, G. Karapetian¹⁸, D. Karlen⁶, V. Kartvelishvili¹⁶, K. Kawagoe²³, T. Kawamoto²³, R.K. Keeler²⁶, R.G. Kellogg¹⁷, B.W. Kennedy²⁰, D.H. Kim¹⁹, K. Klein¹¹, A. Klier²⁴, S. Kluth³², T. Kobayashi²³, M. Kobel³, T.P. Kokott³, S. Komamiya²³, R.V. Kowalewski²⁶, T. Krämer²⁵, T. Kress⁴, P. Krieger⁶, J. von Krogh¹¹, D. Krop¹², T. Kuhl³, M. Kupper²⁴, P. Kyberd¹³, G.D. Lafferty¹⁶, H. Landsman²¹, D. Lanske¹⁴, I. Lawson²⁶, J.G. Layter⁴, A. Leins³¹, D. Lellouch²⁴, J. Letts¹², L. Levinson²⁴, J. Lillich¹⁰, C. Littlewood⁵, S.L. Lloyd¹³, F.K. Loebinger¹⁶, G.D. Long²⁶, M.J. Losty^{6,a}, J. Lu²⁷, J. Ludwig¹⁰, A. Macchiolo¹⁸, A. Macpherson^{28,l}, W. Mader³, S. Marcellini², T.E. Marchant¹⁶, A.J. Martin¹³, J.P. Martin¹⁸, G. Martinez¹⁷, G. Masetti², T. Mashimo²³, P. Mättig²⁴, W.J. McDonald²⁸, J. McKenna²⁷, T.J. McMahon¹, R.A. McPherson²⁶, F. Meijers⁸, P. Mendez-Lorenzo³¹, W. Menges²⁵, F.S. Merritt⁹, H. Mes^{6,a}, A. Michelini², S. Mihara²³, G. Mikenberg²⁴, D.J. Miller¹⁵, S. Moed²¹, W. Mohr¹⁰, T. Mori²³, A. Mutter¹⁰, K. Nagai¹³, I. Nakamura²³, H.A. Neal³³, R. Nisius⁸, S.W. O'Neale¹, A. Oh⁸, A. Okpara¹¹, M.J. Oreglia⁹, S. Orito²³, C. Pahl³², G. Pásztor^{8,i}, J.R. Pater¹⁶, G.N. Patrick²⁰, J.E. Pilcher⁹, J. Pinfold²⁸, D.E. Plane⁸, B. Poli², J. Polok⁸, O. Pooth⁸, M. Przybycień^{8,d}, A. Quadt³, K. Rabbertz⁸, C. Rembser⁸, P. Renkel²⁴, H. Rick⁴, N. Rodning²⁸, J.M. Roney²⁶, S. Rosati³, K. Roscoe¹⁶, Y. Rozen²¹, K. Runge¹⁰, D.R. Rust¹², K. Sachs⁶, T. Saeki²³, O. Sahr³¹, E.K.G. Sarkisyan^{8,m}, C. Sbarra²⁶, A.D. Schaile³¹, O. Schaile³¹, P. Scharff-Hansen⁸, M. Schröder⁸, M. Schumacher²⁵, C. Schwick⁸, W.G. Scott²⁰, R. Seuster^{14,g}, T.G. Shears^{8,j}, B.C. Shen⁴, C.H. Shepherd-Themistocleous⁵, P. Sherwood¹⁵, A. Skuja¹⁷, A.M. Smith⁸, G.A. Snow¹⁷, R. Sobie²⁶, S. Söldner-Rembold^{10,e}, S. Spagnolo²⁰, F. Spano⁹, M. Sproston²⁰, A. Stahl³, K. Stephens¹⁶, D. Strom¹⁹, R. Ströhmer³¹, L. Stumpf²⁶, B. Surrow²⁵, S. Tarem²¹, M. Tasevsky⁸, R.J. Taylor¹⁵, R. Teuscher⁹, J. Thomas¹⁵, M.A. Thomson⁵, E. Torrence¹⁹,

D. Toya²³, T. Trefzger³¹, A. Tricoli², I. Trigger⁸, Z. Trócsányi^{30,f}, E. Tsur²²,
M.F. Turner-Watson¹, I. Ueda²³, B. Ujvári^{30,f}, B. Vachon²⁶, C.F. Vollmer³¹, P. Vannerem¹⁰,
M. Verzocchi¹⁷, H. Voss⁸, J. Vossebeld⁸, D. Waller⁶, C.P. Ward⁵, D.R. Ward⁵, P.M. Watkins¹,
A.T. Watson¹, N.K. Watson¹, P.S. Wells⁸, T. Wengler⁸, N. Wermes³, D. Wetterling¹¹
G.W. Wilson¹⁶, J.A. Wilson¹, T.R. Wyatt¹⁶, S. Yamashita²³, V. Zacek¹⁸, D. Zer-Zion^{8,k}

¹School of Physics and Astronomy, University of Birmingham, Birmingham B15 2TT, UK

²Dipartimento di Fisica dell' Università di Bologna and INFN, I-40126 Bologna, Italy

³Physikalisches Institut, Universität Bonn, D-53115 Bonn, Germany

⁴Department of Physics, University of California, Riverside CA 92521, USA

⁵Cavendish Laboratory, Cambridge CB3 0HE, UK

⁶Ottawa-Carleton Institute for Physics, Department of Physics, Carleton University, Ottawa,
Ontario K1S 5B6, Canada

⁸CERN, European Organisation for Nuclear Research, CH-1211 Geneva 23, Switzerland

⁹Enrico Fermi Institute and Department of Physics, University of Chicago, Chicago IL 60637,
USA

¹⁰Fakultät für Physik, Albert Ludwigs Universität, D-79104 Freiburg, Germany

¹¹Physikalisches Institut, Universität Heidelberg, D-69120 Heidelberg, Germany

¹²Indiana University, Department of Physics, Swain Hall West 117, Bloomington IN 47405,
USA

¹³Queen Mary and Westfield College, University of London, London E1 4NS, UK

¹⁴Technische Hochschule Aachen, III Physikalisches Institut, Sommerfeldstrasse 26-28, D-
52056 Aachen, Germany

¹⁵University College London, London WC1E 6BT, UK

¹⁶Department of Physics, Schuster Laboratory, The University, Manchester M13 9PL, UK

¹⁷Department of Physics, University of Maryland, College Park, MD 20742, USA

¹⁸Laboratoire de Physique Nucléaire, Université de Montréal, Montréal, Quebec H3C 3J7,
Canada

¹⁹University of Oregon, Department of Physics, Eugene OR 97403, USA

²⁰CLRC Rutherford Appleton Laboratory, Chilton, Didcot, Oxfordshire OX11 0QX, UK

²¹Department of Physics, Technion-Israel Institute of Technology, Haifa 32000, Israel

²²Department of Physics and Astronomy, Tel Aviv University, Tel Aviv 69978, Israel

²³International Centre for Elementary Particle Physics and Department of Physics, University
of Tokyo, Tokyo 113-0033, and Kobe University, Kobe 657-8501, Japan

²⁴Particle Physics Department, Weizmann Institute of Science, Rehovot 76100, Israel

²⁵Universität Hamburg/DESY, II Institut für Experimental Physik, Notkestrasse 85, D-
22607 Hamburg, Germany

²⁶University of Victoria, Department of Physics, P O Box 3055, Victoria BC V8W 3P6,
Canada

²⁷University of British Columbia, Department of Physics, Vancouver BC V6T 1Z1, Canada

²⁸University of Alberta, Department of Physics, Edmonton AB T6G 2J1, Canada

²⁹Research Institute for Particle and Nuclear Physics, H-1525 Budapest, P O Box 49, Hungary

³⁰Institute of Nuclear Research, H-4001 Debrecen, P O Box 51, Hungary

³¹Ludwigs-Maximilians-Universität München, Sektion Physik, Am Coulombwall 1, D-85748 Garching, Germany

³²Max-Planck-Institute für Physik, Föhring Ring 6, 80805 München, Germany

³³Yale University, Department of Physics, New Haven, CT 06520, USA

^a and at TRIUMF, Vancouver, Canada V6T 2A3

^b and Royal Society University Research Fellow

^c and Institute of Nuclear Research, Debrecen, Hungary

^d and University of Mining and Metallurgy, Cracow

^e and Heisenberg Fellow

^f and Department of Experimental Physics, Lajos Kossuth University, Debrecen, Hungary

^g and MPI München

ⁱ and Research Institute for Particle and Nuclear Physics, Budapest, Hungary

^j now at University of Liverpool, Dept of Physics, Liverpool L69 3BX, UK

^k and University of California, Riverside, High Energy Physics Group, CA 92521, USA

^l and CERN, EP Div, 1211 Geneva 23

^m and Tel Aviv University, School of Physics and Astronomy, Tel Aviv 69978, Israel.

1 Introduction

The classical way to investigate the structure of the photon at e^+e^- colliders is the measurement of the process

$$e^+(p_1)e^-(p_2) \rightarrow e^+(p'_1)e^-(p'_2) X, \quad (1)$$

proceeding via the interaction of two photons, which can be either quasi-real, γ , or virtual, γ^* . The terms in brackets represent the four-vectors of the particles as shown in Fig. 1.

Depending on the virtualities of the photons the scattered electrons¹ may be observed in the detector. In the case where none of the electrons is observed (anti-tagged), the structure of the quasi-real photon has been studied by OPAL in terms of total cross-sections [1], jet production [2], and charm production [3]. If only one electron is observed (single-tagged), the process can be described as deep-inelastic electron scattering off a quasi-real photon. These events have been studied by OPAL to measure the QED and QCD photon structure functions [3–6]. If both electrons are observed (double-tagged), the dynamics of highly virtual photon collisions is probed. The QED structure of the interactions of two highly virtual photons has already been studied by OPAL [4]. In the analysis presented here, the investigation is extended to the measurement of the hadronic structure. The results are based on data recorded by the OPAL experiment at LEP in the years 1998 to 2000 at e^+e^- centre-of-mass energies of $\sqrt{s_{ee}} = 189 - 209$ GeV, using events where both scattered electrons are observed in the small-angle silicon-tungsten (SW) luminometer. The measured differential

¹Electrons and positrons are generically referred to as electrons.

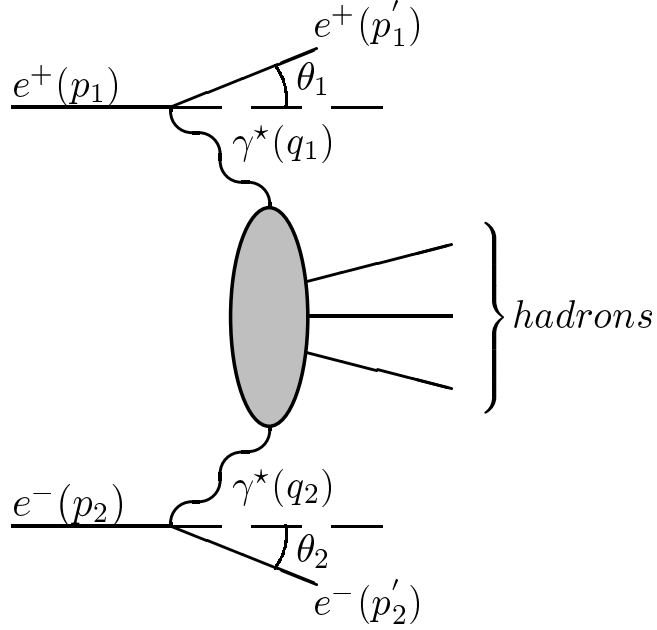


Figure 1: The diagram corresponding to the process $e^+e^- \rightarrow e^+e^- \text{ hadrons}$.

cross-sections are compared to the prediction of the Quark Parton Model (QPM), to a NLO calculation [7] of the process $e^+e^- \rightarrow e^+e^- q\bar{q}$, to the PHOJET Monte Carlo model [8] and to BFKL [9] calculations [10–12]. A similar analysis has been published by the L3 Collaboration [13] using data taken at $\sqrt{s_{ee}} = 91$ GeV and $\sqrt{s_{ee}} = 183$ GeV.

2 Theoretical framework

In this paper double-tagged events are studied, i.e. both final state electrons are scattered at sufficiently large polar angles² θ_i to be observed in the detector. This corresponds to the situation where both radiated photons which take part in the hard scattering process, are highly virtual. Throughout the paper, $i = 1, 2$ denotes quantities which are connected with the upper and lower vertex in Fig. 1, respectively.

The virtualities of the radiated photons are given by $Q_i^2 = -(p_i - p'_i)^2 > 0$. The usual dimensionless variables of deep inelastic scattering are defined as:

$$y_1 = \frac{q_1 q_2}{p_1 q_2}, \quad y_2 = \frac{q_1 q_2}{p_2 q_1}, \quad (2)$$

²The right-handed OPAL coordinate system is defined with the z axis pointing in the direction of the e^- beam and the x axis pointing towards the centre of the LEP ring. The polar angle θ , the azimuthal angle ϕ and the radius r are the usual spherical coordinates.

$$x_1 = \frac{Q_1^2}{2q_1 q_2}, \quad x_2 = \frac{Q_2^2}{2q_1 q_2}. \quad (3)$$

The e^+e^- centre-of-mass energy squared is given by $s_{ee} = (p_1 + p_2)^2$ and the hadronic invariant mass squared by $W^2 = (q_1 + q_2)^2$.

The kinematical variables Q_i^2 , y_i and x_i are obtained from the four-vectors of the tagged electrons and the hadronic final state via:

$$Q_i^2 = 2E_b E_i (1 - \cos \theta_i), \quad (4)$$

$$y_i = 1 - \frac{E_i}{E_b} \cos^2(\theta_i/2), \quad (5)$$

$$x_i = \frac{Q_i^2}{Q_1^2 + Q_2^2 + W^2}, \quad (6)$$

where E_b refers to the energy of the beam electrons, and the mass m_e of the electron has been neglected.

In this analysis, the hadronic invariant mass, W , is obtained from the energies, E_h , and momenta, \vec{p}_h , of final state hadrons (h), excluding the scattered electrons:

$$W^2 = \left(\sum_h E_h \right)^2 - \left(\sum_h \vec{p}_h \right)^2 = E_{\text{had}}^2 - \vec{p}_{\text{had}}^2. \quad (7)$$

For the comparison of the data to BFKL calculations the following additional kinematic quantity, which is a measure of the length of the gluon ladder, is defined [14]:

$$Y = \ln \left(\frac{s_{ee} y_1 y_2}{\sqrt{Q_1^2 Q_2^2}} \right) \simeq \ln \left(\frac{W^2}{\sqrt{Q_1^2 Q_2^2}} \right) = \bar{Y}, \quad (8)$$

where the approximation requires $W^2 \gg Q_i^2$. In the analysis presented here Y will be approximated by \bar{Y} .

The differential cross-section for the process of Eq. 1 in the limit $Q_i^2 \gg m_e^2$ and for small values of y_i is given by [15]

$$\begin{aligned} d^6\sigma &= \frac{d^3\mathbf{p}'_1 d^3\mathbf{p}'_2}{E'_1 E'_2} \mathcal{L}_{\text{TT}} \left(\sigma_{\text{TT}} + \sigma_{\text{LT}} + \sigma_{\text{TL}} + \sigma_{\text{LL}} + \frac{1}{2} \tau_{\text{TT}} \cos 2\bar{\phi} - 4\tau_{\text{TL}} \cos \bar{\phi} \right) \\ &= \frac{d^3\mathbf{p}'_1 d^3\mathbf{p}'_2}{E'_1 E'_2} \mathcal{L}_{\text{TT}} \sigma_{\gamma^*\gamma^*}, \end{aligned} \quad (9)$$

$$L_{\text{TT}} = \int \frac{d^3\mathbf{p}'_1 d^3\mathbf{p}'_2}{E'_1 E'_2} \mathcal{L}_{\text{TT}}, \quad (10)$$

where $\bar{\phi}$ is the angle between the two scattering planes of the electrons in the photon-photon centre-of-mass system. The cross-sections σ_{TT} , σ_{TL} , σ_{LT} and σ_{LL} and the interference terms τ_{TT} and τ_{TL} correspond to specific helicity states of the interacting photons (T=transverse

and L=longitudinal). The sum of these terms is $\sigma_{\gamma^*\gamma^*}$, the cross-section for the reaction $\gamma^*\gamma^* \rightarrow \text{hadrons}$. The process $e^+e^- \rightarrow e^+e^- \text{hadrons}$ can be written as a product of a term describing the flux of the incoming photons and the cross-section for the interaction of the virtual photons. For any bin L_{TT} is derived by integrating over the phase space of the outgoing electrons. Here L_{TT} describes the flux of transversely polarised photons, and only depends on the four-vectors q_1, q_2, p_1, p_2 and on the mass of the electron [16].

In the case of lepton pair production $e^+e^- \rightarrow e^+e^- \ell^+\ell^-$ the cross-section is completely determined by QED. For hadronic final states QCD corrections have to be taken into account and in addition the cross-sections and interference terms cannot be completely calculated within the framework of perturbative QCD. For $\mu^+\mu^-$ final states [4] it is found that the contributions from τ_{TT} and τ_{TL} are large for $Q_1^2 \approx Q_2^2$ and small values of W^2 . It cannot be excluded that the interference terms and contributions from longitudinal photons in the QCD case are also large [16]. Therefore, only comparisons to theoretical models containing predictions for all cross-sections and interference terms are meaningful. The cleanest experimental quantity which can be extracted without making further assumptions about the interference terms is the cross-section for the reaction $e^+e^- \rightarrow e^+e^- \text{hadrons}$ as given in Eq. 9. Dividing by L_{TT} the cross-section $\sigma_{\gamma^*\gamma^*}$ can be extracted.

The order α_s QCD radiative corrections to the process $e^+e^- \rightarrow e^+e^- q\bar{q}$ have also been calculated [7]. The calculation accounts for the running of α_s and α and allows for the evaluation of differential cross-sections for several variables, but, it is valid only for massless quarks. The LO result is somewhat higher than the QPM prediction, which is expected due to the use of massless quarks. Overall the NLO corrections are predicted to be small, but they change e.g. the shape of the \overline{Y} distribution, as can be seen from Table 1.

Recently, much attention has been given to the BFKL pomeron [9], especially for small Bjorken- x deep-inelastic electron-proton (ep) scattering at HERA. With increasing centre-of-mass energies squared, s , and for moderate photon virtualities, large logarithms in $1/x$ are expected to affect the rise of the cross-section. Resummation of these logarithms leads to the so-called BFKL evolution equation from which one derives that the total ep cross-section should increase as s^{α_0} with $\alpha_0 \sim 0.5$ in Leading Order (LO), where α_0 denotes the pomeron intercept. The onset of such BFKL effects has been searched for in ep structure function and hadronic final state data [17]. The situation is so far still inconclusive, with the strongest hint for BFKL effects in the data coming from the analysis of forward π^0 production.

It has been argued [14, 18–20] that e^+e^- collider offer an excellent opportunity to test the BFKL prediction, through a measurement of $\sigma_{\gamma^*\gamma^*}$. For sufficiently large photon virtualities Q_1^2 and Q_2^2 (i.e. more than a few GeV 2), this BFKL calculation can be carried out without non-perturbative input. If additionally $Q_1^2 \simeq Q_2^2$, then the evolution in Q^2 is suppressed, allowing for a clean test of BFKL effects. This condition is to a good approximation fulfilled for the data sample selected in this paper.

The leading-log resummation for $\gamma^*\gamma^*$ scattering, can be represented by the so-called ‘gluon ladder diagrams’, as sketched in Fig. 2. The first diagram is the $\gamma\gamma \rightarrow q\bar{q}$ contribution and the next ones give the gluon exchange contributions. The original LO-BFKL

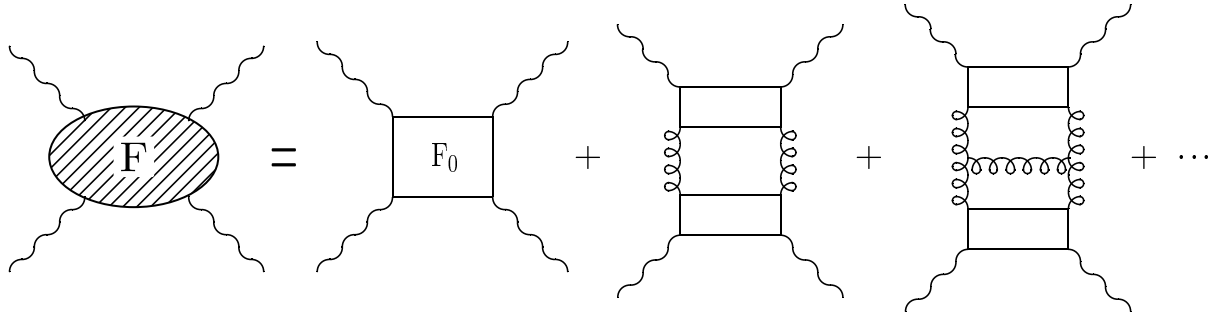


Figure 2: Diagrams contributing to the leading $\ln 1/x$ approximation for the $\gamma^*\gamma^*$ cross-section.

calculations [14] predicted an increase of $\sigma_{\gamma^*\gamma^*}$ by a factor 20 or more compared to calculations without BFKL effects, or with only DGLAP (Q^2) evolution [21]. Since then the LO-BFKL calculations have been improved by including charm quark mass effects, running of the strong coupling constant α_s and the contribution of the longitudinal photon polarisation states. Recently, it has become clear that the Next-to-Leading Order (NLO) corrections to the BFKL equation are large and effectively reduce the value of α_0 . A phenomenological determination of the Higher Order (HO) effects was presented in Ref. [20] and the resulting BFKL scattering cross-sections were shown to increase by a factor 2-3 only, relative to the calculations without BFKL effects. Since then theoretically motivated improved higher order calculations have been performed [11, 12, 22–26], and give similar results.

3 Monte Carlo generators

Several Monte Carlo generators have been compared to the data or have been used to correct the data for detector effects. Most relevant to the analysis presented here are the programs which are used to model two-photon interactions for double-tagged, single-tagged and anti-tagged events. The main features of the programs are briefly described here. For further details the reader is referred to the original publications. An overview can be found in [16].

The PHOJET event generator has been used to simulate double-tagged events. There are significant differences between PHOJET1.10 and the previous version PHOJET1.05 in several aspects of the event generation, the latter producing e.g. larger cross-sections at large W . In this paper we compare with the most recent and improved version of the program PHOJET1.10. The program is based on the Dual Parton Model, containing both hard and soft processes [8]. The hard processes are calculated in LO perturbative QCD, and soft processes are modelled based on γp , $p p$ and $p \bar{p}$ data assuming Regge factorisation. The $\gamma^*\gamma^*$ cross-section is obtained from the $\gamma\gamma$ cross-section by extrapolating in Q^2 on the basis of the Generalised Vector Dominance model using the description of Ref. [27]. Events are generated

for both soft and hard partonic processes. A cut-off on the transverse momentum of the scattered partons in the photon-photon centre-of-mass system of 2.5 GeV is used to separate the two classes of events. For this reason the generation of events with W below 5 GeV is known to be incomplete. As a cross-check of the PHOJET model the PYTHIA6.130 [28] Monte Carlo generator, based on a recent model by Friberg and Sjöstrand [29], is used for the simulation of double-tagged two-photon events.

The general purpose Monte Carlo program HERWIG5.9+ k_t (dyn) [30] was used to simulate single-tagged two-photon events. This model version uses a modified transverse momentum distribution, k_t , for the quarks inside the photon, with the upper limit dynamically (dyn) adjusted according to the hardest scale in the event, which is of order Q^2 . This has been found [31] to give a better description of the experimentally observed hadronic final states.

The PHOJET1.10 Monte Carlo has also been used to simulate anti-tagged two-photon events. It is known to describe satisfactorily the OPAL anti-tagged two-photon data [1].

The QPM cross-section $e^+e^- \rightarrow e^+e^-q\bar{q}$, which corresponds to the diagram labelled F_0 in Fig. 2, was calculated with the GALUGA [32] program, which includes all terms from Eq. 9. The quark masses assumed are 0.325 GeV for uds and 1.5 GeV for c quarks. For the region of $W > 5$ GeV considered here, the cross-section depends only weakly on the chosen masses, e.g. the results for u and c quarks differ only slightly. GALUGA was also used to calculate L_{TT} .

Radiative corrections are calculated with the program BDK [33]. As for the GALUGA Monte Carlo, the BDK program calculates the QPM cross-section with, in addition, initial and final state QED radiative corrections to the scattered electrons. It has been verified that the non-radiative cross-sections predicted by BDK and GALUGA agree with each other. GALUGA has more flexibility for calculating cross-sections and is therefore used to calculate the L_{TT} factors and QPM predictions. The size of the radiative corrections depends on the variables used to calculate the kinematics, and also to some extent on the non-radiative cross-section.

Fig. 3 compares two methods of calculating the variable \bar{Y} . The first method uses the hadronic final state to calculate W . The second method is a hybrid that calculates W using y_1 and y_2 obtained from the electrons, if both are positive and at least one y_i is larger than 0.25 otherwise \bar{Y} is calculated as for the first method. The non-radiative QPM cross-section was reweighted to the leading order PHOJET cross-section, which agrees well with the measured cross-section (see Section 7). Fig. 3 shows the ratio of the non-radiative (Born) to the full radiative, detector level measured (rad) cross-section. For the fully hadronic method the radiative corrections are small. However, for the electron method the corrections can be larger than 50% at large \bar{Y} values. Obviously, measurements based on the electron kinematics cannot be compared with models or BFKL calculations in the region $\bar{Y} > 4$, unless radiative corrections have been applied. Since the actual size of the radiative corrections also depends on the non-radiative cross-section itself, an iterative procedure would be required to extract the non-radiative cross-section. The present statistics do not permit such a procedure, so in

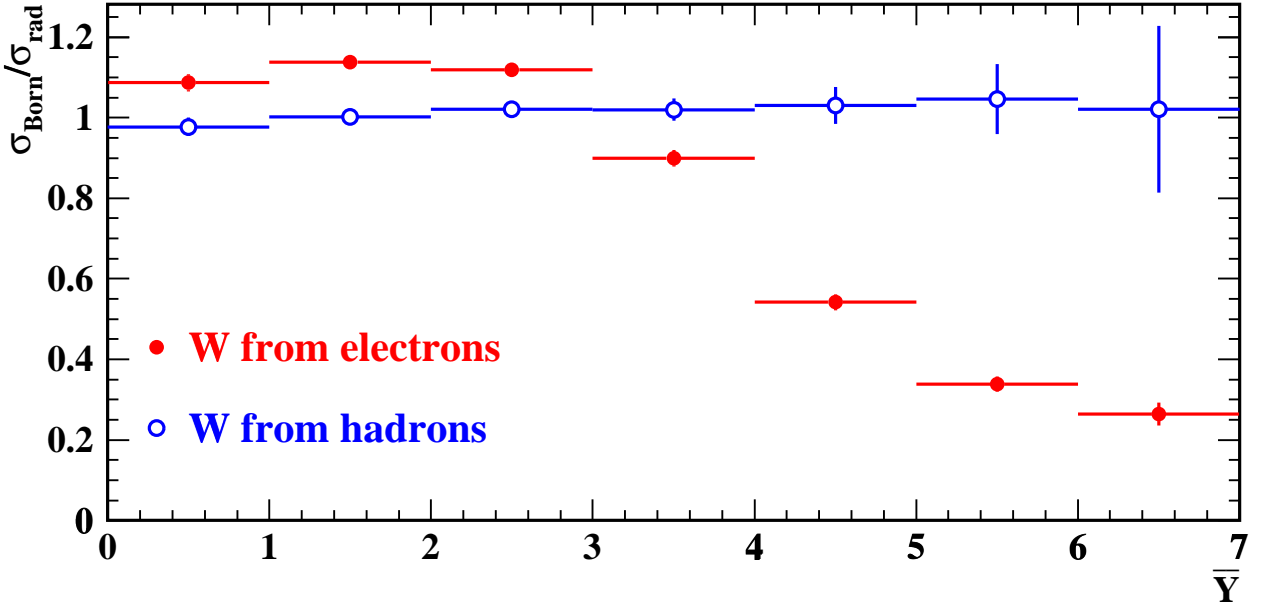


Figure 3: Radiative corrections for the process $e^+e^- \rightarrow e^+e^- \text{ hadrons}$ as a function of \bar{Y} for two different methods to calculate W : a combined electron/hadronic final state method (electrons), and a purely hadronic final state method (hadrons), as explained in the text. Only statistical errors are shown.

the analysis which follows \bar{Y} has been calculated only with the hadronic variables, for which the corrections are much smaller.

4 The OPAL detector

A detailed description of the OPAL detector can be found in Ref. [34]. Here only a brief account of the main components relevant to the present analysis is given.

The central tracking system is located inside a solenoid magnet which provides a uniform axial magnetic field of 0.435 T along the beam axis. The central tracking system consists of a two-layer silicon micro-vertex detector [35], a high precision vertex drift chamber, a large volume jet chamber and a set of z -chambers for accurately measuring track coordinates along the beam direction. The transverse momenta, p_T , of tracks are measured with a precision of $\sigma_{p_T}/p_T = \sqrt{0.02^2 + (0.0015 \cdot p_T)^2}$ (p_T in GeV).

The central detector is surrounded in the barrel region ($|\cos \theta| < 0.82$) by a lead glass electromagnetic calorimeter (ECAL) and a hadronic sampling calorimeter (HCAL). Outside the HCAL, the detector is surrounded by muon chambers. There are similar layers of detectors in the end caps ($0.81 < |\cos \theta| < 0.98$). The barrel and end cap sections of the ECAL

are both constructed from lead glass blocks, with a depth of 24.6 radiation lengths in the barrel region and more than 22 radiation lengths in the endcaps.

The small angle region from 47 to 140 mrad around the beam pipe on both sides of the interaction point is covered by the forward detectors (FD) and the region from 25 to 59 mrad by the silicon-tungsten luminometers (SW) [36]. The lower boundary of the SW acceptance is effectively 33 mrad due to the installation of a low-angle shield to protect the central detector from synchrotron radiation.

The FD consists of cylindrical lead-scintillator calorimeters with a depth of 24 radiation lengths divided azimuthally into 16 segments. The electromagnetic energy resolution is approximately $18\%/\sqrt{E}$, where E is in GeV.

The SW detector consists of two cylindrical small angle calorimeters encircling the beam pipe at approximately ± 2.5 m from the interaction point. Each calorimeter is made of a stack of 18 tungsten plates, interleaved with 19 layers of silicon sampling wafers and mounted as two interlocking C-shaped modules around the LEP beam pipe. The depth of the detector amounts to 22 radiation lengths. Each silicon layer consists of 16 wedge-shaped silicon detectors. The sensitive area of the calorimeter fully covers radii between 81 and 142 mm from the beam axis. The energy resolution is approximately 5% on both sides. It is found that the energy resolution is almost constant with the energy due to energy leakage and dead material. In this analysis, the SW detector was used for tagging the scattered electrons from the process $e^+e^- \rightarrow e^+e^-$ hadrons.

5 Event selection

The data sample used in this analysis corresponds to an integrated luminosity of 592.9 pb^{-1} accumulated by the OPAL experiment in 1998 (168.5 pb^{-1}), 1999 (208.3 pb^{-1}) and 2000 (216.1 pb^{-1}) at e^+e^- centre-of-mass energies $\sqrt{s_{ee}} = 189 - 209$ GeV with a luminosity weighted average of $\sqrt{s_{ee}} = 198$ GeV. Double-tagged two-photon events were selected with the following set of cuts:

1. Two electron candidates should be observed, one in each SW detector, with energies $E_{1,2} > 0.4E_b$ and polar angles in the range $34 < \theta_{1,2} < 55$ mrad. The angles $\theta_{1,2}$ are measured with respect to the original beam direction. On each side the calorimeter cluster with the highest energy is taken as the electron candidate. The energy threshold for the electron candidates is kept as low as possible in order to access large W values, where BFKL effects may become significant.
2. In order to remove events with scattered electrons in FD or in the central electromagnetic calorimeter, we require that there is no single cluster in these detectors with an energy above $0.25E_b$.
3. At least 3 tracks ($N_{\text{ch}} \geq 3$) have to be found in the tracking system. A track is required

to have a minimum transverse momentum of 120 MeV, and to fulfill standard quality cuts as given in [37].

4. The visible invariant mass, W_{vis} , is required to be larger than 5 GeV. It is reconstructed from tracks measured in the central tracking detectors and the position and energy of clusters measured in the electromagnetic and hadronic calorimeters, as well as in the forward detectors FD. A matching algorithm [37] is used to avoid double counting of the particle momenta in the calorimeters and tracking chambers.
5. To reduce the background due to beam–gas interactions, the z position of the primary vertex $|\langle z_0 \rangle|$ is required to be less than 4 cm from the nominal interaction point. Here $\langle z_0 \rangle$ is calculated as the error weighted average of the z coordinates of all tracks at the point of closest approach to the origin in the r, ϕ plane. The standard requirement that the distance of any track to the origin of the z axis should be less than 30 cm was not applied in order to keep all possible tracks including those from off-momentum electrons interacting with the beam pipe. We also require that the distance of the primary vertex from the beam axis should be less than 0.5 cm.
6. In order to ensure that the event is well contained in the detector and to reduce background from beam–gas interactions, it is required that the z component of the total momentum vector of the event, $|\sum p_z|$ is less than 35 GeV, and that the total energy measured in the event is less than $2.2E_b$.
7. Remaining Bhabha-like events (i.e. a Bhabha event with random overlap of hadronic activity) are tagged using the back-to-back topology of the scattered electrons, if both have an energy larger than $0.7E_b$. Events are rejected if the difference in radius, Δr and difference in azimuthal angle, $\Delta\phi$ of the position of the two clusters in the laboratory reference frame are $|\Delta r| < 0.5$ cm and $(\pi - 0.1) < |\Delta\phi| < \pi$ rad.

With these cuts 175 events are selected in the data. Among these we expect background events from two main sources. The first contribution is from e^+e^- processes containing electrons in the final state and the second stems from coincidences of e^+e^- processes without electrons in the final state with off-momentum electrons from beam–gas interactions.

The background from e^+e^- reactions containing electrons in the final state, which amounts to 18.3 events, dominantly stems from the processes $e^+e^- \rightarrow e^+e^-\tau\bar{\tau}$ and $e^+e^- \rightarrow e^+e^-e^+e^-$, and was estimated using the Vermaseren Monte Carlo program [38]. The contribution from other e^+e^- background, such as $e^+e^- \rightarrow q\bar{q}$ and other processes leading to four fermion final states was found to be negligible, as was the background from single-tagged two-photon processes with a cluster from the hadronic final state misidentified as the second electron.

Beam–gas interactions can result in off-momentum electrons observed in the SW detectors, faking final state electrons from the process $e^+e^- \rightarrow e^+e^-$ hadrons. This background was estimated using a sample of Bhabha events, selected by requiring events with two back-to-back electrons in the SW calorimeters, which each have an energy of more than $0.7E_b$, with $|\Delta r| < 0.5$ cm and $(\pi - 0.1) < |\Delta\phi| < \pi$ rad. Additional clusters in the SW detectors, which fulfill the criteria for electron candidates mentioned above, but do not belong

to the Bhabha event, are counted as off-momentum electrons. The probabilities to have an overlapping off-momentum electron with an event coming from the interaction region are determined for the left ($-z$) / right ($+z$) side of the detector separately and amount to 0.000715/0.00115 (1998), 0.00139 /0.00279 (1999) and 0.00117 /0.000671 (2000). The relative statistical precision of these probabilities is 2-3%. The background expectation is more than a factor two larger in 1999 than in the other years. Using these numbers, and assuming that the overlap probabilities are independent between the left and right side of the detector, we predict that there should be 14.6 events with 'double' overlaps in the Bhabha sample, which agrees well with the 19 events observed.

It is essential to check this method of estimating the background from off-momentum electrons on a different process. Here we used a sample of single-tagged two-photon events. The sample is selected with the same cuts as described for the double-tagged selection, except that only one scattered electron is required and cuts 6) and 7) are not applied. The event properties are compared with the absolute prediction for the single-tagged plus background events. The single-tagged events are based on the HERWIG generator with the GRV [39] parametrisation of the photon structure function F_2 , which has been shown to describe the single-tagged cross-section [6] within about 10% for $E > 0.7E_b$. The genuine single-tagged events are complemented by the physics background and by artificially created single-tagged events constructed by a combination of anti-tagged two-photon events generated by PHOJET with a cluster created by an off-momentum electron. The θ , ϕ and energy dependence of the electron clusters are given by the spectra of the additional clusters in Bhabha events.

Fig. 4 shows the 1999 data, which is expected to have the largest background from off-momentum overlaps, compared with the prediction resulting from the sum of HERWIG and the background, normalised to the luminosity of the data. Results are shown for θ , ϕ and energy of the scattered electron normalised to the energy of the beam electrons. Fig. 5 shows separately for the 1998, 1999 and 2000 data samples, the missing longitudinal momentum and missing transverse momentum in the event, calculated including the untagged electron, which has been assumed to have zero transverse momentum and an energy equal to the energy of the beam electrons. Both distributions have been normalised to the energy of the beam electrons. For energies below $0.6E_b$ the off-momentum background clearly dominates and the observed angular dependences, especially in ϕ , clearly follow the expected shape.

The agreement between data and prediction is very good for all variables examined, providing confidence that the background from overlap off-momentum beam electrons is under control to a level of about 10%. The off-momentum background estimate was used to calculate the contribution of fake double-tagged events, resulting from the overlap of one background cluster with a single-tagged two-photon event and the overlap of two background clusters with an untagged event. In total 4.3, 15.2 and 4.6 overlap events are predicted for the 1998, 1999 and 2000 data samples. After subtraction of all backgrounds 132.6 events remain, with each year contributing with 31.9 ± 6.5 (1998), 63.5 ± 9.3 (1999) and 37.2 ± 7.0 (2000) events, whereas 42.5, 53.7 and 55.5 events are predicted by PHOJET. The difference between the number of events observed in the three years is of the order of twice their statistical error. Since the statistics of this measurement are small, the data of all years will

be combined in the following.

The double-tagged events are triggered by two groups of independent triggers. The first trigger is based on the energy deposits of the observed electrons in the SW calorimeters. The second group only relies on the observed tracks and clusters from the hadronic final state. Based on these two independent groups, the trigger efficiency of the hadronic final state alone, for events with two electrons with energies above $0.4E_b$, has been determined from the data to be $(96 \pm 4)\%$.

6 Properties of double-tagged $\gamma^*\gamma^*$ events

A PHOJET Monte Carlo sample is used to correct the data for acceptance and resolution effects. It is therefore essential that the shape of all important distributions is well reproduced by the Monte Carlo simulation. In this Section a comparison is made of data distributions with predictions from PHOJET. Variables calculated from the scattered electrons as well as variables calculated from the hadronic final state are studied. The integrated luminosity of the Monte Carlo sample amounts to approximately 40 times that of the data. All Monte Carlo distributions shown in this Section are normalised to the data luminosity. In all plots involving both sides of the SW detector, the sum of the distributions obtained separately for each side is shown.

In Fig. 6 variables which are based on electron quantities, and the variables $x_{1,2}$, are compared with predictions of PHOJET and background estimates. All variables, the normalised electron energies $E_{1,2}$, the polar angles $\theta_{1,2}$, the azimuthal angles $\phi_{1,2}$, and photon virtualities $Q_{1,2}^2$, are reasonably well described by the sum of the signal as predicted by PHOJET and the estimated background from overlaps with off-momentum electrons and other physics processes. Note that PHOJET does not contain any explicit effects from BFKL, which would show up in the region of low electron energies. Fig. 6e) shows the logarithm of the ratio of the photon virtualities, $\ln(Q_1^2/Q_2^2)$, of the two photons in an event. This distribution is peaked around zero, indicating that the Q^2 values of both photons are generally close to one another, which is ideal to test for BFKL effects.

In Fig. 7 distributions are shown which characterise the hadronic final state in double-tagged two-photon events: the number of tracks, N_{ch} , the visible hadronic invariant mass, W_{vis} , the hadronic energy, E_{had} , the variable \overline{Y} as well as the sum of the longitudinal $\sum p_z$ and transverse $\sum p_T$ momenta. Within statistics, the agreement with PHOJET is reasonable.

7 Results

The cross-section for the process $e^+e^- \rightarrow e^+e^- \text{ hadrons}$ has been measured in the kinematic region defined by the scattered electron energies $E_{1,2} > 0.4E_b$, the polar angles in the range

$34 < \theta_{1,2} < 55$ mrad with respect to either beam direction, and $W > 5$ GeV. Differential cross-sections are presented as a function of x , Q^2 , W , and the azimuthal correlation between the two electrons $\Delta\phi$. Here Q^2 refers to the maximum of Q_1^2 and Q_2^2 , and x is the corresponding value of x_1 or x_2 . For the comparison with BFKL predictions we also present the differential cross-section as a function of \bar{Y} . From the measurement of the differential cross-sections of the process $e^+e^- \rightarrow e^+e^-$ hadrons we extract the cross-sections for the reaction $\gamma^*\gamma^* \rightarrow$ hadrons as a function of the variable under study, using L_{TT} , obtained separately for each bin using Monte Carlo. Technically this was done by setting $\sigma_{\gamma^*\gamma^*} \equiv 1$ in GALUGA and integrating (Eq. 9) using only L_{TT} for each bin within the experimental phase space restrictions. The cross-sections for the reaction $\gamma^*\gamma^* \rightarrow$ hadrons predicted by the models are calculated using the same L_{TT} factors. For all variables except Q^2 the results for the cross-sections of the reaction $\gamma^*\gamma^* \rightarrow$ hadrons are given at an average value of Q^2 , $\langle Q^2 \rangle = 17.9$ GeV 2 . Due to limited statistics in the data, a simple bin-by-bin method was applied to correct for detector and selection inefficiencies. The efficiency, R_e , and purity, R_p , are defined as:

$$R_e = \frac{N^{\text{Det} \otimes \text{Had}}}{N^{\text{Had}}} \quad R_p = \frac{N^{\text{Det} \otimes \text{Had}}}{N^{\text{Det}}}$$

where $N^{\text{Det} \otimes \text{Had}}$ is the number of events which are generated in a bin and measured in the same bin, N^{Had} is the number of events which are generated in a bin and N^{Det} is the number of events measured in a bin. In both definitions the terms ‘generated’ and ‘measured’ denote events which pass all selection cuts at the hadron or at the detector level, respectively. The correction factor $N^{\text{Had}}/N^{\text{Det}}$ is obtained by dividing purity by efficiency. For the W variable the purity is typically around 60% over the whole range, and the efficiency is in the range of 30-50%. Similar numbers are obtained for \bar{Y} and x , while for the $\Delta\phi$ and Q^2 variables the efficiencies are around 60% and purities around 80%. The correction factor is typically around 1.5 and fairly constant.

The systematic error of the measurement has been evaluated taking into account several contributions. All changes, except the change of the cut on N_{ch} , are applied to the Monte Carlo event samples because of low statistics of the data.

1. The error due to a possible shift of the energy scale of the SW detectors was taken into account by scaling the electron energy by $\pm 1\%$, in accord with the uncertainty in the scale observed in single-tagged events, which is conservative because the differences observed for Bhabha events were much smaller.
2. The uncertainty in the description of the energy scale of the central electromagnetic calorimeter ECAL was taken into account by varying the energy scale by $\pm 3\%$ [6].
3. To estimate the uncertainties due to the selection cuts, we have performed the following checks, reflecting the resolution of the variables:
 - (a) The lower cut on $\theta_{1,2}$ was changed from 34 mrad by ± 0.4 mrad.
 - (b) The lower cut on $E_{1,2}$ was changed by $\pm 5\%$.

- (c) The cut on W was changed by ± 0.5 GeV.
 - (d) The cut on $|\langle z_0 \rangle|$ was changed by ± 1.0 cm.
 - (e) The cut on the distance of the primary vertex from the beam axis was changed by ± 0.1 cm.
4. The PYTHIA Monte Carlo was used instead of PHOJET to correct the data. The differences between the models are generally within 10-15%, except for the high W region where the difference amounts to 25%. The full differences were taken as the errors.
5. In modelling the region of $W < 5$ GeV PHOJET is incomplete. This affects the measurement only through migrations from lower to higher values of W . To estimate the influence of the imperfect modelling of that region in PHOJET we have chosen the following method. The cross-section for events with $W < 5$ GeV have been rescaled such that there was a smooth transition in the W distribution around $W = 5$ GeV. Then the number of events generated for $W < 5$ GeV were varied by $\pm 50\%$.
6. The uncertainty in the estimation of the off-momentum background was taken to be 10% of the background, motivated by the level of agreement observed for the single-tagged events.
7. The cut on the number of charged tracks has been changed from $N_{\text{ch}} \geq 3$ to $N_{\text{ch}} \geq 4$. This change has been applied simultaneously to data and Monte Carlo.
8. The 4% uncertainty in the trigger efficiency was added to the total systematic error.

The total systematic error was obtained by adding in quadrature errors coming from the above checks, where the sum has been performed separately for positive and negative contributions. The main contributions to the systematic errors come from changing the Monte Carlo model from PHOJET to PYTHIA (-16% change in the total cross-section), changing the cut on N_{ch} (-12%), and varying the lower cuts on W ($\pm 8\%$) and $\theta_{1,2}$ ($\pm 5\%$). The normalisation uncertainty due to the luminosity measurement is less than 1% and has been neglected.

The total measured cross-section for the process $e^+e^- \rightarrow e^+e^-$ hadrons in the previously defined phase space, is 0.35 ± 0.04 (stat) $^{+0.04}_{-0.08}$ (sys) pb. The expected cross-section from PHOJET is 0.39 ± 0.02 (stat) pb, while the GALUGA prediction for QPM using massive quarks is 0.27 ± 0.02 (stat) pb, and the NLO predictions for the reaction $e^+e^- \rightarrow e^+e^- q\bar{q}$ using massless quarks is 0.35 pb. In Fig. 8 we show the measured differential cross-section for the processes $e^+e^- \rightarrow e^+e^-$ hadrons and the cross-section for $\gamma^*\gamma^* \rightarrow$ hadrons as a function of x and Q^2 . The numerical values are given in Tables 2 and 3. PHOJET better describes the data at lower x values, where the QPM prediction is too low. In contrast, in the large x region the QPM prediction is sufficient to account for the data.

Fig. 9 shows the measured cross-sections as a function of W and $\Delta\phi$. The model predictions indicate a slightly different shape than is observed for the data. Studies for HERA

have shown [40] that angular variables similar to $\Delta\phi$ can be sensitive to the presence of BFKL dynamics, but so far no calculations are available for $\gamma^*\gamma^*$ scattering. The data show that the $\Delta\phi$ behaviour of the cross-section for the reaction $e^+e^- \rightarrow e^+e^-$ hadrons is flat, while the cross-section for the process $\gamma^*\gamma^* \rightarrow$ hadrons increases from $\Delta\phi = 0$ to $\Delta\phi = \pi$. PHOJET1.10 does not describe the $\Delta\phi$ distribution, whereas QPM reproduces the shape of the distribution. One should remark that the earlier version, PHOJET1.05, follows the data in both shape and normalisation.

In Fig. 10 we compare the measured cross-section for the processes $e^+e^- \rightarrow e^+e^-$ hadrons and $\gamma^*\gamma^* \rightarrow$ hadrons as a function of \bar{Y} with the PHOJET Monte Carlo, the QPM calculation, the NLO calculation for the reaction $e^+e^- \rightarrow e^+e^- q\bar{q}$, and numerical BFKL calculations (Tables 2 and 3). The BFKL predictions are shown for the LO-BFKL [10] and a NLO-BFKL [11] calculation both using Y . Also shown is a (partial) HO-BFKL calculation [12] using \bar{Y} . All BFKL predictions are shown for Y or $\bar{Y} > 2$, except for the NLO-BFKL calculation which has been evaluated for $Y > 1$. Both PHOJET and QPM using massive quarks describe the data equally well. Also the NLO calculation for the reaction $e^+e^- \rightarrow e^+e^- q\bar{q}$, evaluated for five massless quarks and using $\Lambda_5^{\overline{\text{MS}}} = 0.2275$ GeV, is in accord with the data. As can be seen from Table 1 the predicted differential cross-sections as functions of Y and \bar{Y} are very different at small values, but get much closer at higher values. This is expected from the approximation made in Eq. 8. It means that at low values of \bar{Y} the comparison of the experimental result with predictions based on Y is rather uncertain, whereas at high values the uncertainty from using different definitions is small.

For all BFKL predictions shown the cross-section is significantly larger than the PHOJET prediction for $\bar{Y} > 3$, and the differences increase with increasing \bar{Y} . The LO-BFKL calculation predicts a cross-section which is too large compared to the data. This LO-BFKL calculation (Bartels99) [10] already incorporates improvements compared to the original results [14] by including effects of the charm quark mass, the running of the strong coupling constant α_s and contribution of longitudinal photon polarisation states. Hence BFKL effects as large as predicted by the LO-BFKL calculation are not in agreement with the data. BFKL cross-sections have been calculated to NLO (Kim99) [11], using the BLM [41] optimal scale setting. At the highest \bar{Y} value the NLO-BFKL cross-section is a factor seven larger than the PHOJET prediction. The data lie in between these two predictions. Finally, the calculation (Kwiecinski) [12] contains the dominant contribution of the higher order corrections via the so-called consistency constraint, to all orders. Its prediction in the highest reachable \bar{Y} range is about a factor two lower than for the NLO-BFKL calculation, and this prediction and PHOJET are roughly equally compatible with the data.

8 Summary and conclusions

A data sample collected by the OPAL experiment at LEP based on an integrated luminosity of 592.9 pb^{-1} and for e^+e^- centre-of-mass energies $\sqrt{s_{ee}} = 189 - 209$ GeV has been used to study interactions of virtual photons. Differential cross-sections for the processes $e^+e^- \rightarrow$

e^+e^- hadrons are measured as functions of x , Q^2 , W , $\Delta\phi$ and \bar{Y} . From this, the cross-sections for the reaction $\gamma^*\gamma^* \rightarrow$ hadrons as a functions of these variables have been derived. Both PHOJET1.10 and QPM describe the data equally well for the cross-sections in x , Q^2 , W , and \bar{Y} . PHOJET1.10 does not describe the $\Delta\phi$ distribution, whereas QPM reproduces the shape of the distribution. Also the NLO calculation for the reaction $e^+e^- \rightarrow e^+e^- q\bar{q}$ is in accord with the data.

Within current calculations BFKL effects could lead to an increase of the cross-section by a factor up to 20 for the largest \bar{Y} values. The data rule out BFKL cross-sections which are as large as those predicted by LO-BFKL and NLO-BFKL calculations as presented in [11]. Calculations including dominant higher order corrections predict smaller effects in the LEP range and are found to be consistent with the measured cross-sections. The limited statistics and available \bar{Y} range of the data prevent establishing or ruling out the onset of BFKL dynamics in this reaction.

Acknowledgements:

We are grateful to C. Ewerz, V. Kim, J. Kwiecinski and L. Motyka for providing their predictions. We wish to thank S. Frixione for providing the software to calculate the NLO predictions.

We particularly wish to thank the SL Division for the efficient operation of the LEP accelerator at all energies and for their continuing close cooperation with our experimental group. We thank our colleagues from CEA, DAPNIA/SPP, CE-Saclay for their efforts over the years on the time-of-flight and trigger systems which we continue to use. In addition to the support staff at our own institutions we are pleased to acknowledge the Department of Energy, USA,
National Science Foundation, USA,
Particle Physics and Astronomy Research Council, UK,
Natural Sciences and Engineering Research Council, Canada,
Israel Science Foundation, administered by the Israel Academy of Science and Humanities,
Minerva Gesellschaft,
Benoziyo Center for High Energy Physics,
Japanese Ministry of Education, Science and Culture (the Monbusho) and a grant under the Monbusho International Science Research Program,
Japanese Society for the Promotion of Science (JSPS),
German Israeli Bi-national Science Foundation (GIF),
Bundesministerium für Bildung und Forschung, Germany,
National Research Council of Canada,
Research Corporation, USA,
Hungarian Foundation for Scientific Research, OTKA T-029328, T023793 and OTKA F-023259.

References

- [1] OPAL Collaboration, G. Abbiendi et al., Eur. Phys. J. **C14** (2000) 199.
- [2] OPAL Collaboration, G. Abbiendi et al., Eur. Phys. J. **C10** (1999) 547.
- [3] OPAL Collaboration, G. Abbiendi et al., Eur. Phys. J. **C16** (2000) 579.
- [4] OPAL Collaboration, G. Abbiendi et al., Eur. Phys. J. **C11** (1999) 409.
- [5] OPAL Collaboration, K. Ackerstaff et al., Phys. Lett. **B412** (1997) 225;
OPAL Collaboration, K. Ackerstaff et al., Phys. Lett. **B411** (1997) 387;
OPAL Collaboration, K. Ackerstaff et al., Z. Phys. **C74** (1997) 33.
- [6] OPAL Collaboration, G. Abbiendi et al., Eur. Phys. J. **C18** (2000) 15.

- [7] M. Cacciari et al., *QCD radiative corrections to $\gamma^*\gamma^* \rightarrow \text{hadrons}$* , hep-ph/0011368.
- [8] R. Engel, Z. Phys. **C66** (1995) 203;
R. Engel and J. Ranft, Phys. Rev. **D54** (1996) 4246.
- [9] E.A. Kuraev, L.N. Lipatov and V.S. Fadin, Sov. Phys. JETP **45** (1977) 199;
Ia. Balitski and L.N. Lipatov, Sov. J. Nucl. Phys. **28** (1978) 822.
- [10] J. Bartels, C. Ewerz and R. Staritzbichler, Phys. Lett. **B492** (2000) 56.
- [11] S.J. Brodsky et al., JETP Lett. **70** (1999) 155;
V. Kim, private communication.
- [12] J. Kwiecinski and L. Motyka, Phys. Lett. **B462** (1999) 203.
- [13] L3 Collaboration, M. Acciarri et al., Phys. Lett. **B453** (1999) 333.
- [14] J. Bartels, A. De Roeck and H. Lotter, Phys. Lett. **B389** (1996) 742;
J. Bartels, A. De Roeck, H. Lotter and C. Ewerz, DESY preprint 97-123E, *The $\gamma^*\gamma^*$ Total Cross-Section and the BFKL pomeron at the 500 GeV e^+e^- Linear Collider*, hep-ph/9710500;
S.J. Brodsky, F. Hautmann and D.E. Soper, Phys. Rev. **D56** (1997) 6957.
- [15] V.M. Budnev, I.F. Ginzburg, G.V. Meledin and V.G. Serbo, Phys. Rep. **15** (1975) 181.
- [16] R. Nisius, Phys. Rep. **332** (2000) 165.
- [17] ZEUS Collaboration, J. Breitweg et al., Eur. Phys. J. **C6** (1999) 239;
H1 Collaboration, C. Adloff et al., Nucl. Phys. **B538** (1999) 3;
H1 Collaboration, C. Adloff et al., Phys. Lett. **B462** (1999) 440.
- [18] S.J. Brodsky, F. Hautmann and D.E. Soper, Phys. Rev. Lett. **78** (1997) 803.
- [19] A. Białas, W. Czyż and W. Florkowski, Eur. Phys. J. **C2** (1998) 683.
- [20] M. Boonekamp, A. De Roeck, C. Royon and S. Wallon, Nucl. Phys. **B555** (1999) 540.
- [21] G. Altarelli and G. Parisi, Nucl. Phys. **B126** (1977) 298;
V.N. Gribov and L.N. Lipatov, Sov. J. Nucl. Phys. **15** (1972) 438;
L.N. Lipatov, Sov. J. Nucl. Phys. **20** (1975) 94;
Y.L. Dokshitzer, Sov. Phys. JETP. **46** (1977) 641.
- [22] M. Ciafaloni, D. Colferai and G.P. Salam, Phys. Rev. **D60** (1999) 114036;
M. Ciafaloni, D. Colferai, Phys. Lett. **B452** (1999) 372.
- [23] C.R. Schmidt, Phys. Rev. **D60** (1999) 074003.
- [24] J.R. Forshaw, D.A. Ross and A. Saboi Vera, Phys. Lett. **B455** (1999) 273.
- [25] R.S. Thorne, Phys. Rev. **D60** (1999) 054031.

- [26] G. Altarelli, R.D. Ball and S. Forte, Nucl. Phys. **B599** (2001) 383.
- [27] I.F. Ginzburg and V.G. Serbo, Phys. Lett. **B109** (1982) 231.
- [28] T. Sjöstrand, Comp. Phys. Comm. **82** (1994) 74;
T. Sjöstrand, LUND University Report, LU-TP-95-20 (1995).
- [29] C. Friberg and T. Sjöstrand, JHEP **09** (2000) 010.
- [30] G. Marchesini et al., Comp. Phys. Comm. **67** (1992) 465.
- [31] The LEP Working Group for Two-Photon Physics, ALEPH, L3 and OPAL Collaborations, *Comparison of Deep Inelastic Electron-Photon Scattering Data with the HERWIG and PHOJET Monte Carlo Models*, CERN-EP-2000-109, hep-ex/0010041.
- [32] G.A. Schuler, Comp. Phys. Comm. **108** (1998) 279.
- [33] F.A. Berends, P.H. Daverveldt and R. Kleiss, Nucl. Phys. **B253** (1985) 421; Comp. Phys. Comm. **40** (1986) 271; Comp. Phys. Comm. **40** (1986) 285; Nucl. Phys. **B264** (1986) 243.
- [34] OPAL Collaboration, K. Ahmet et al., Nucl. Instr. Meth. **A305** (1991) 275.
- [35] P.P. Allport et al., Nucl. Instr. Meth. **A324** (1993) 34.
- [36] M. Hauschild et al., Nucl. Instr. Meth. **A379** (1996) 436.
- [37] OPAL Collaboration, G. Alexander et al., Phys. Lett. **B377** (1996) 181.
- [38] J.A.M. Vermaasen, Nucl. Phys. **B229** (1983) 347.
- [39] M. Glück, E. Reya and A. Vogt, Phys. Rev. **D45** (1992) 3986;
M. Glück, E. Reya and A. Vogt, Phys. Rev. **D46** (1992) 1973.
- [40] J. Bartels, V. Del Duca and M. Wüsthoff, Z. Phys. **C76** (1997) 75.
- [41] S.J. Brodsky, G.P. Lepage and P.B. Mackenzie, Phys. Rev. **D28** (1983) 228.

range	$d\sigma/d\bar{Y}$		$d\sigma/dY$	
	LO	NLO	LO	NLO
0 – 1	0.071	0.065	0.015	0.014
1 – 2	0.135	0.128	0.149	0.138
2 – 3	0.087	0.089	0.111	0.122
3 – 4	0.041	0.047	0.047	0.053
4 – 6	0.010	0.013	0.011	0.014

Table 1: Predictions for the differential cross-section for the process $e^+e^- \rightarrow e^+e^- q\bar{q}$ as functions of \bar{Y} and Y using the calculation from [7].

$\langle x \rangle$	range	N_{ev}	$\frac{d\sigma}{dx}$ OPAL [pb]	Statistical error	Systematic error		$\frac{d\sigma}{dx}$ PHOJET [pb]
					up	down	
0.06	0.0 - 0.1	45.6	1.46	0.27	0.11	0.26	1.29
0.15	0.1 - 0.2	50.1	1.22	0.20	0.10	0.19	1.26
0.26	0.2 - 0.35	34.9	0.55	0.11	0.11	0.20	0.85

$\langle Q^2 \rangle$ [GeV 2]	range [GeV 2]	N_{ev}	$\frac{d\sigma}{dQ^2}$ OPAL [pb/GeV 2]	Statistical error	Systematic error		$\frac{d\sigma}{dQ^2}$ PHOJET [pb/GeV 2]
					up	down	
13.6	10 - 16	32.3	0.016	0.003	0.002	0.003	0.018
18.9	16 - 22	59.4	0.026	0.004	0.003	0.006	0.027
24.4	22 - 27	25.0	0.013	0.003	0.001	0.003	0.020

$\langle W \rangle$ [GeV]	range [GeV]	N_{ev}	$\frac{d\sigma}{dW}$ OPAL [pb/GeV]	Statistical error	Systematic error		$\frac{d\sigma}{dW}$ PHOJET [pb/GeV]
					up	down	
7.2	5 - 10	65.1	0.031	0.004	0.0053	0.0098	0.041
12.4	10 - 15	30.6	0.017	0.004	0.0012	0.0015	0.021
20.6	15 - 35	32.5	0.005	0.001	0.0004	0.0010	0.004
41.5	35 - 50	3.4	0.001	0.001	0.0001	0.0001	0.000

$\Delta\phi$ [rad]	range [rad]	N_{ev}	$\frac{d\sigma}{d\Delta\phi}$ OPAL [pb/rad]	Statistical error	Systematic error		$\frac{d\sigma}{d\Delta\phi}$ PHOJET [pb/rad]
					up	down	
0.31	0.00 - 0.63	20.2	0.081	0.022	0.010	0.032	0.195
0.94	0.63 - 1.26	23.7	0.098	0.024	0.012	0.035	0.163
1.57	1.26 - 1.89	31.2	0.130	0.026	0.013	0.036	0.120
2.20	1.89 - 2.51	27.1	0.117	0.026	0.011	0.020	0.083
2.83	2.51 - 3.14	30.4	0.132	0.028	0.009	0.010	0.068

\bar{Y}	range	N_{ev}	$\frac{d\sigma}{dY}$ OPAL [pb]	Statistical error	Systematic error		$\frac{d\sigma}{dY}$ PHOJET [pb]
					up	down	
0.5	0 - 1	25.7	0.059	0.013	0.029	0.033	0.083
1.5	1 - 2	44.9	0.105	0.018	0.007	0.021	0.141
2.5	2 - 3	37.1	0.108	0.020	0.009	0.011	0.111
3.5	3 - 4	12.7	0.040	0.014	0.003	0.009	0.040
5.0	4 - 6	11.1	0.026	0.010	0.003	0.010	0.009

Table 2: The differential cross-section for the process $e^+e^- \rightarrow e^+e^-$ hadrons in the region $E_{1,2} > 0.4E_b$, $34 < \theta_{1,2} < 55$ mrad and $W > 5$ GeV, as a function of x , Q^2 , W , $\Delta\phi$ and \bar{Y} . The average value of x , Q^2 , W and the central value for $\Delta\phi$ and \bar{Y} in a bin, value of the bin boundaries, number of measured events in the bin after background subtraction, value of the differential cross-section with statistical and systematic errors as well as the differential cross-section predicted by PHOJET1.10, are given.

$\langle x \rangle$	σ OPAL [nb]	Statistical error	Systematic error		σ PHOJET [nb]	σ QPM [nb]	L_{TT} 10^{-3}
			up	down			
0.06	4.66	0.85	0.33	0.83	4.11	2.79	0.0314
0.15	8.92	1.42	0.71	1.39	9.18	6.23	0.0137
0.26	5.76	1.10	1.18	2.10	8.95	6.03	0.0143

$\langle Q^2 \rangle$ [GeV 2]	σ OPAL [nb]	Statistical error	Systematic error		σ PHOJET [nb]	σ QPM [nb]	L_{TT} 10^{-3}
			up	down			
13.6	5.63	1.23	0.77	1.05	6.30	4.61	0.0169
18.9	6.37	0.91	0.75	1.56	6.66	4.41	0.0241
24.4	3.91	0.89	0.36	0.98	5.93	4.20	0.0165

$\langle W \rangle$ [GeV]	σ OPAL [nb]	Statistical error	Systematic error		σ PHOJET [nb]	σ QPM [nb]	L_{TT} 10^{-3}
			up	down			
7.2	6.79	0.96	1.17	2.15	9.03	6.27	0.0227
12.4	7.11	1.51	0.52	0.63	9.08	5.38	0.0117
20.6	5.53	1.14	0.38	1.11	4.01	2.95	0.0183
41.5	3.10	2.06	0.29	0.43	1.38	1.27	0.0045

$\Delta\phi$ [rad]	σ OPAL [nb]	Statistical error	Systematic error		σ PHOJET [nb]	σ QPM [nb]	L_{TT} 10^{-3}
			up	down			
0.31	3.18	0.84	0.40	1.25	7.64	2.82	0.0161
0.94	4.25	1.03	0.51	1.53	7.05	3.51	0.0145
1.57	6.84	1.38	0.68	1.88	6.28	4.74	0.0120
2.20	7.44	1.67	0.70	1.25	5.31	5.94	0.0099
2.83	9.56	2.02	0.68	0.76	4.90	6.44	0.0087

\bar{Y}	σ OPAL [nb]	Statistical error	Systematic error		σ PHOJET [nb]	σ QPM [nb]	L_{TT} 10^{-3}
			up	down			
0.5	6.11	1.34	2.95	3.42	8.60	5.37	0.0097
1.5	6.84	1.17	0.43	1.39	9.14	6.59	0.0154
2.5	7.99	1.51	0.69	0.83	8.27	4.98	0.0135
3.5	3.78	1.38	0.32	0.84	3.79	2.98	0.0105
5.0	4.97	1.82	0.49	1.81	1.71	1.40	0.0106

Table 3: The cross-section for the process $\gamma^*\gamma^* \rightarrow \text{hadrons}$ as a function of x , Q^2 , W , $\Delta\phi$ and \bar{Y} . The average value of x , Q^2 , W and the central value for $\Delta\phi$ and \bar{Y} in a bin, value of the cross-section with statistical and systematic errors, the cross-section predicted by PHOJET1.10 and QPM as well as L_{TT} are given.

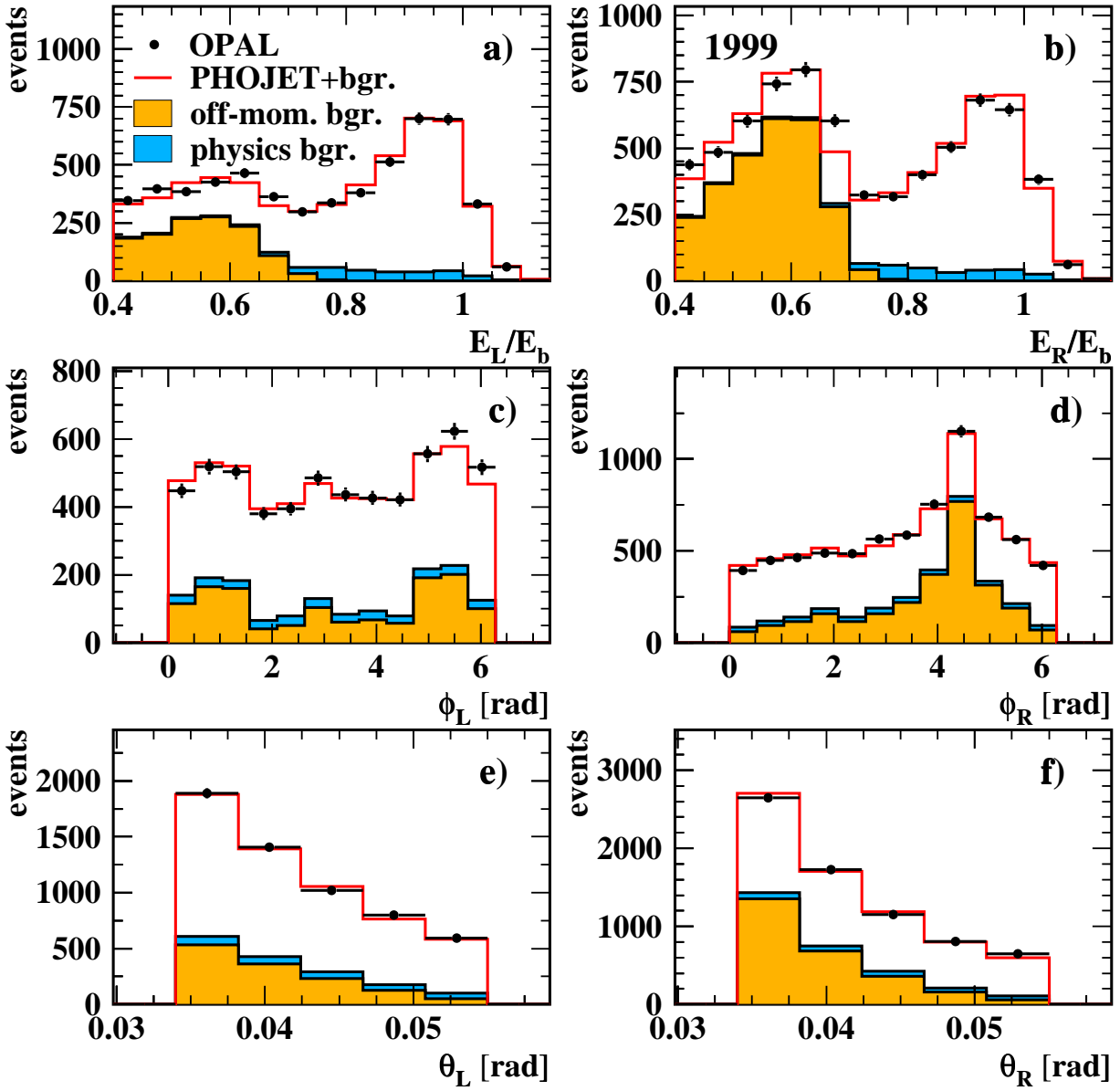


Figure 4: Distributions of the electron energy normalised to the energy of the beam electrons (a,b), electron azimuthal angle (c,d), and electron polar angle (e,f), shown separately for the left (L) and right (R) side of the OPAL detector, for selected single-tagged events in 1999. The histograms are the predictions for the single-tagged process from HERWIG, the off-momentum background contribution, and the background from other physics channels.

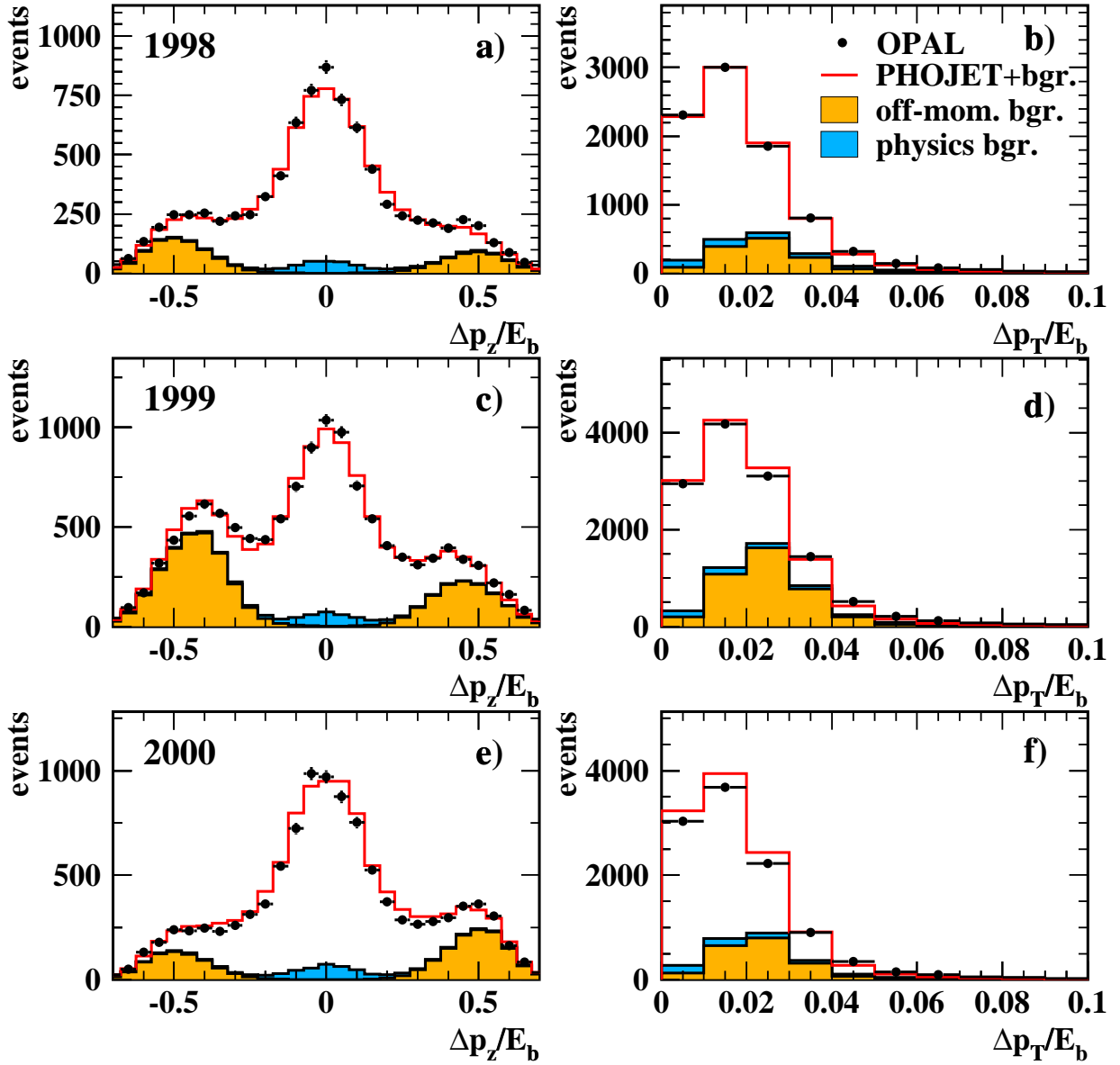


Figure 5: Distributions of the scaled missing longitudinal momentum (a,c,e) and the scaled missing transverse momentum (b,d,f) in single-tagged events for the different years. The meaning of the histograms are as defined in Fig. 4.

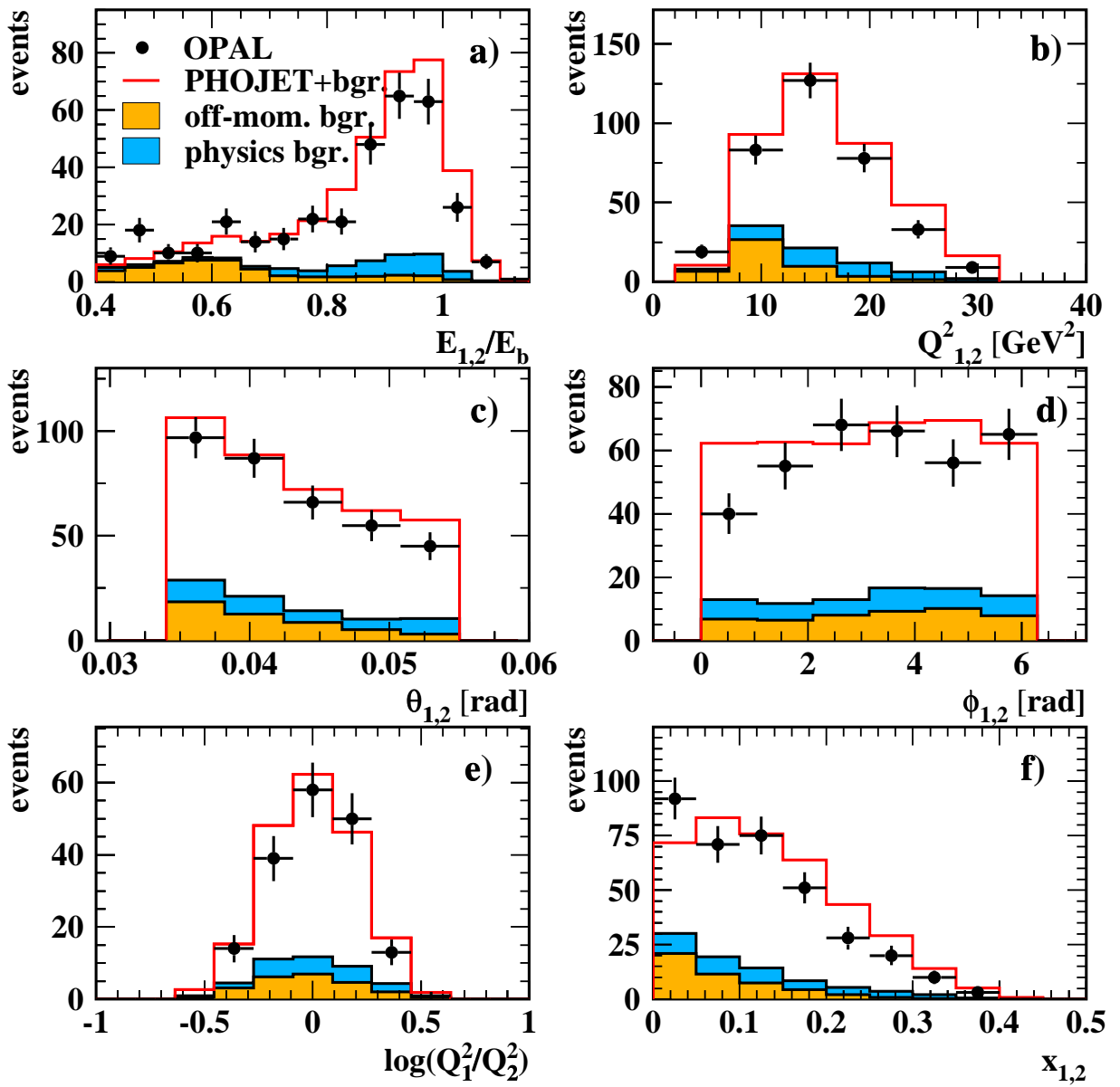


Figure 6: Distributions of (a) the energies of the electrons, normalised to the energy of the beam electrons, (b) the virtualities of both photons, (c) the polar angles of the electrons, (d) the azimuthal angles of the electrons, (e) the ratio of the photon virtualities and (f) the x values of double-tagged two-photon events. The histograms are the predictions for the double-tagged two-photon process from PHOJET1.10, the off-momentum background contribution, and the background from other physics channels.

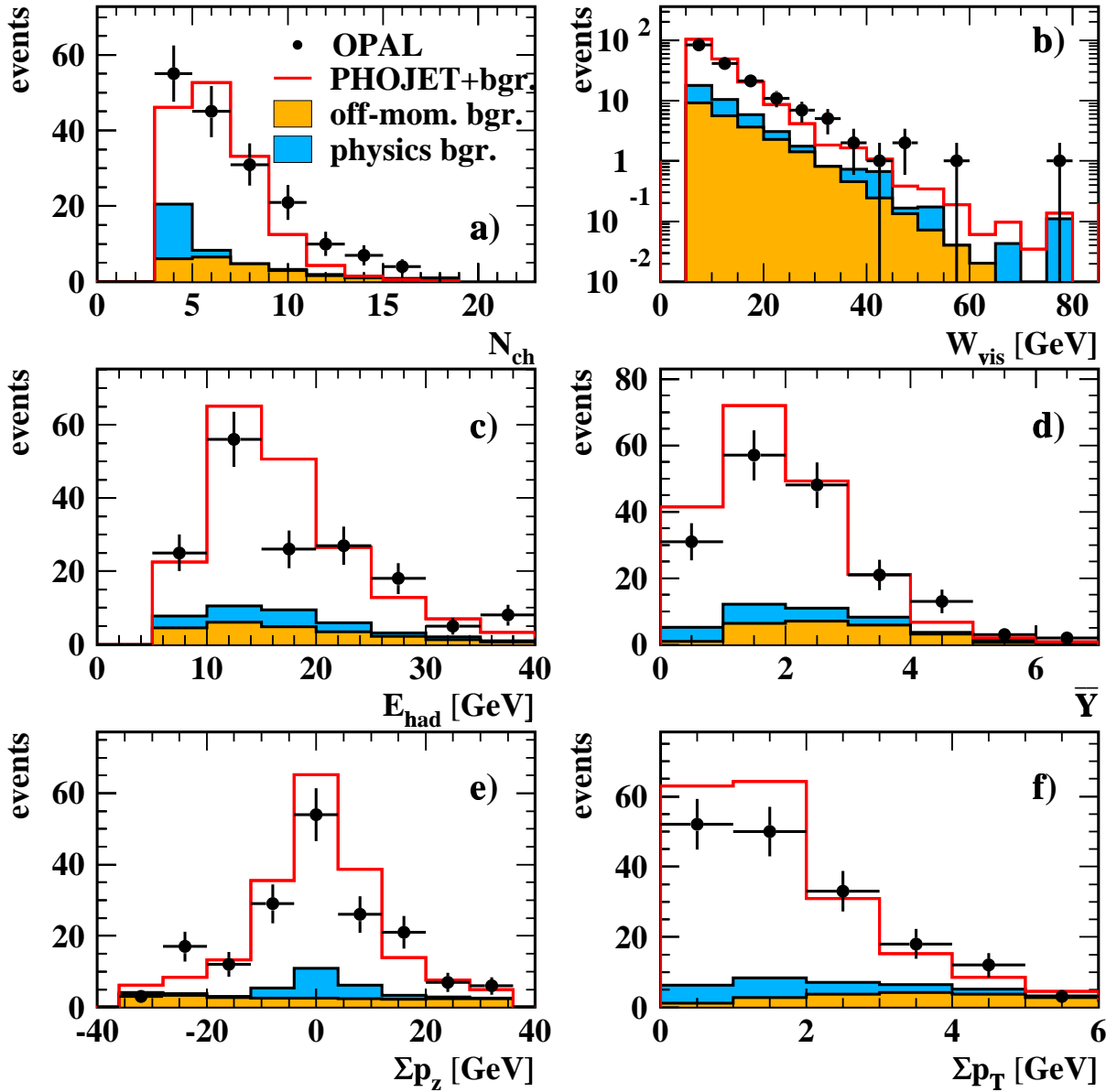


Figure 7: Distributions of (a) the number of tracks of the hadronic final state, (b) the visible hadronic invariant mass, (c) the total hadronic energy (d) the variable \bar{Y} , (e) the missing longitudinal momentum and (f) the missing transverse momentum for double-tagged events. The PHOJET1.10 predictions and backgrounds contributions are as in Fig. 6.

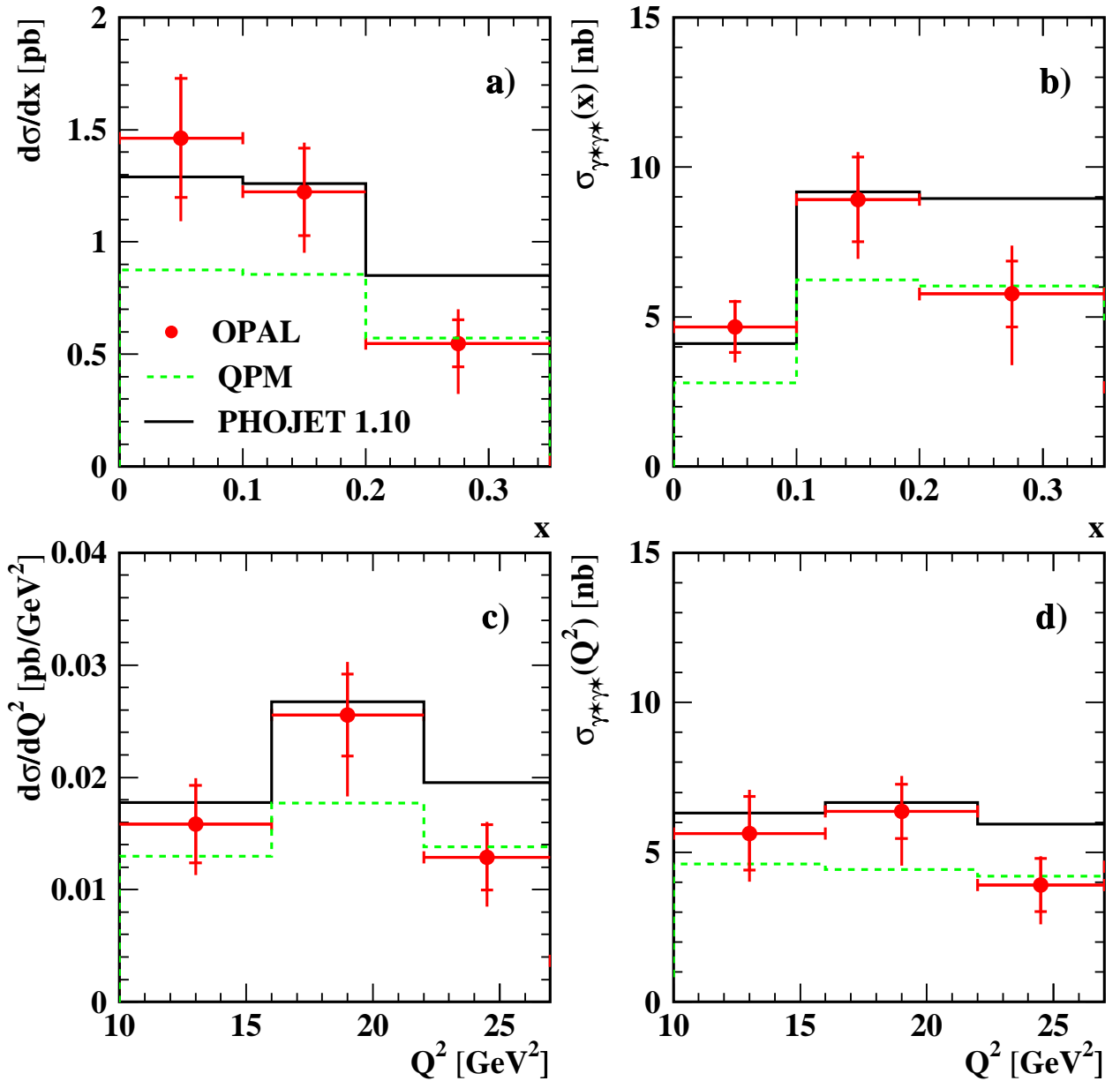


Figure 8: Cross-sections for the process $e^+e^- \rightarrow e^+e^-$ hadrons in the region $E_{1,2} > 0.4E_b$, $34 < \theta_{1,2} < 55$ mrad and $W > 5$ GeV, and for the process $\gamma^*\gamma^* \rightarrow$ hadrons, as functions of x for $\langle Q^2 \rangle = 17.9$ GeV 2 (a,b), and as functions of Q^2 (c,d). Data are shown as full dots in the centre of the bins. The inner error bars represent the statistical errors and the outer error bars represent statistical and systematic errors added in quadrature. The predictions of PHOJET1.10 are shown as solid lines, and those of QPM as dashed lines.

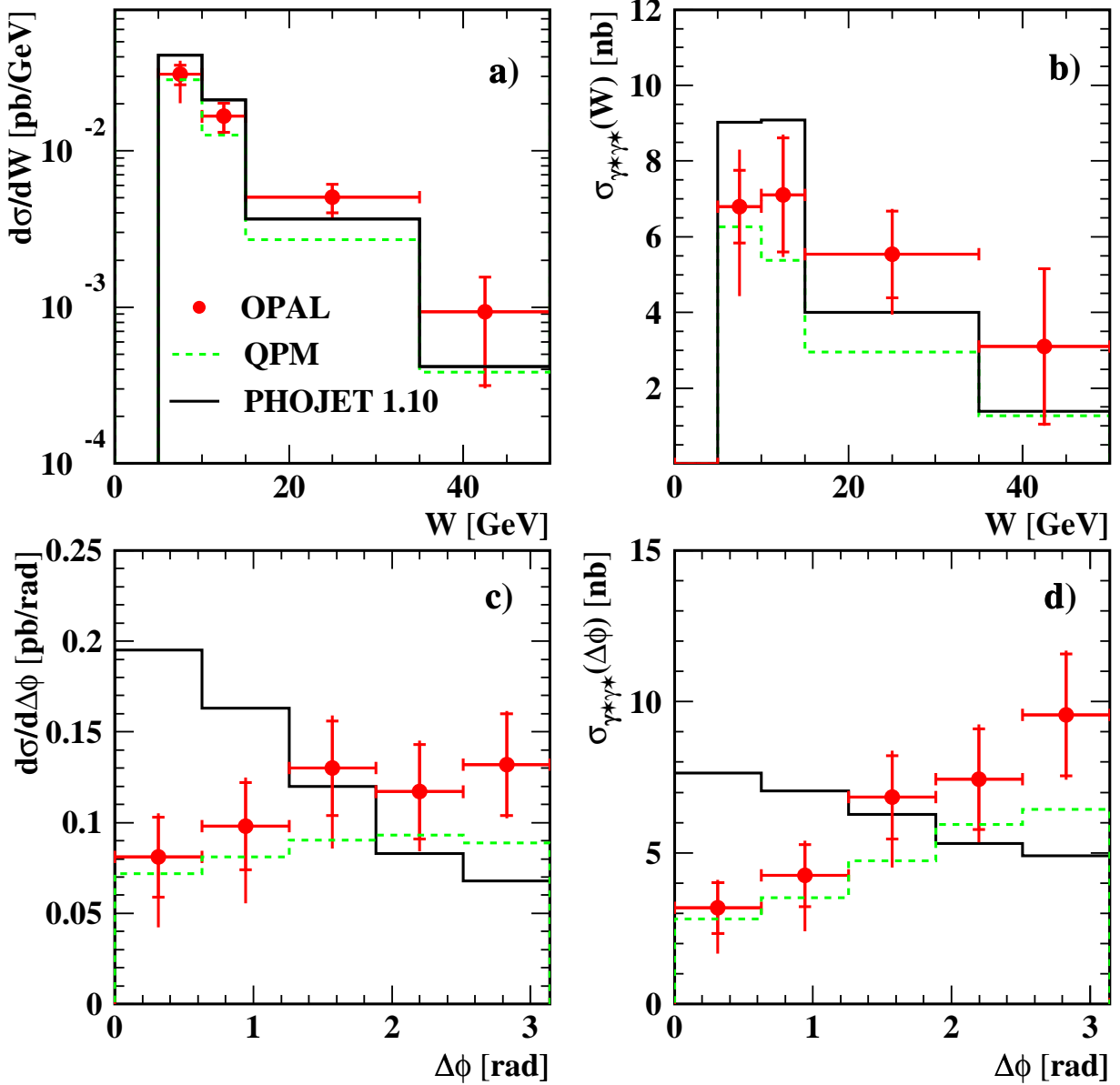


Figure 9: Cross-sections for the process $e^+e^- \rightarrow e^+e^-$ hadrons in the region $E_{1,2} > 0.4E_b$, $34 < \theta_{1,2} < 55$ mrad and $W > 5$ GeV, and for the process $\gamma^*\gamma^* \rightarrow$ hadrons for $\langle Q^2 \rangle = 17.9$ GeV 2 , as functions of W (a,b) and $\Delta\phi$ (c,d). Data are shown as full dots in the centre of the bins. The inner error bars represent the statistical errors and the outer error bars represent statistical and systematic errors added in quadrature. The predictions of PHOJET1.10 are shown as solid lines, and those of QPM as dashed lines.

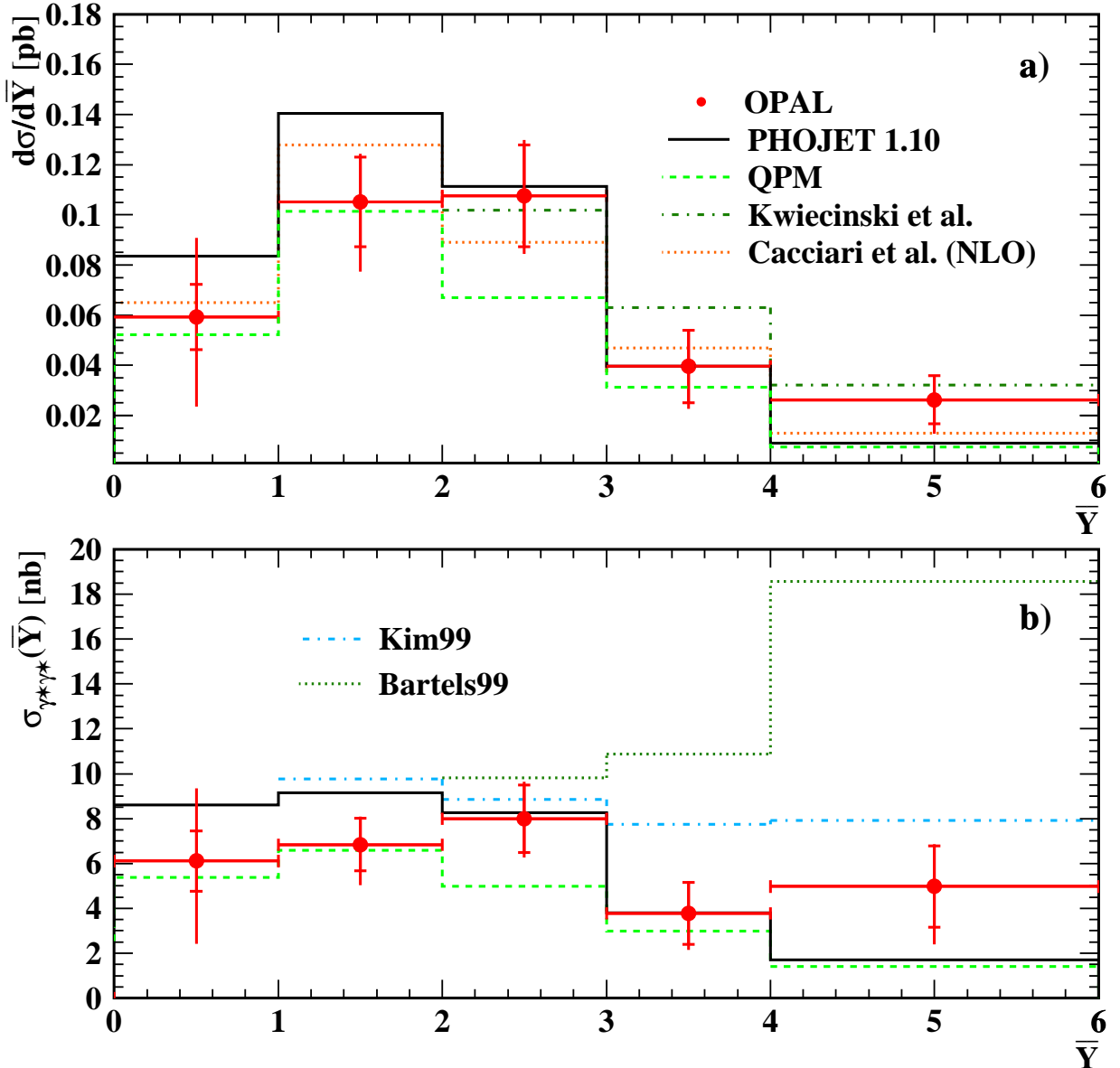


Figure 10: Cross-sections for the process $e^+e^- \rightarrow e^+e^- \text{hadrons}$ in the region $E_{1,2} > 0.4E_b$, $34 < \theta_{1,2} < 55$ mrad and $W > 5$ GeV, and the process $\gamma^*\gamma^* \rightarrow \text{hadrons}$ for $\langle Q^2 \rangle = 17.9$ GeV^2 , as functions of \bar{Y} . Data are shown as full dots in the centre of the bins. The inner error bars represent the statistical errors and the outer error bars represent statistical and systematic errors added in quadrature. The predictions of PHOJET1.10 are shown as the solid lines, that of the NLO calculation of the process $e^+e^- \rightarrow e^+e^- q\bar{q}$ as dotted lines, and those of QPM as dashed lines. Three BFKL calculations are shown: a LO one from Bartels et al. (Bartels99), NLO from Kim et al. (Kim99) using Y , and the calculation from Kwiecinski et al., using the consistency constraint calculated for \bar{Y} .